Nanoscale Heating of an Ultrathin Oxide Film Studied by Tip-Enhanced Raman Spectroscopy

Shuyi Liu,[1] Martin Wolf,[1] and Takashi Kumagai[1,2,*]
[1]Department of Physical Chemistry, Fritz-Haber Institute of the Max-Planck Society, Faradayweg 4-6, 14195 Berlin, Germany
[2]Center for Mesoscopic Sciences, Institute for Molecular Science, Okazaki 444-8585, Japan

(Received 7 December 2020; revised 13 March 2022; accepted 11 April 2022; published 17 May 2022)

We report on the nanoscale heating mechanism of an ultrathin ZnO film using low-temperature tip-enhanced Raman spectroscopy. Under the resonance condition, intense Stokes and anti-Stokes Raman scattering can be observed for the phonon modes of a two-monolayer (ML) ZnO on an Ag(111) surface, enabling us to monitor local heating at the nanoscale. It is revealed that the local heating originates mainly from inelastic electron tunneling through the electronic resonance when the bias voltage exceeds the conduction band edge of the 2-ML ZnO. When the bias voltage is lower than the conduction band edge, the local heating arises from two different contributions, namely direct optical excitation between the interface state and the conduction band of 2-ML ZnO or injection of photoexcited electrons from an Ag tip into the conduction band. These optical heating processes are promoted by localized surface plasmon excitation. Simultaneous mapping of tip-enhanced Raman spectroscopy and scanning tunneling spectroscopy for 2-ML ZnO including an atomic-scale defect demonstrates visualizing a correlation between the heating efficiency and the local density of states, which further allows us to analyze the local electron-phonon coupling strength with ~2 nm spatial resolution.

DOI: 10.1103/PhysRevLett.128.206803

Heating is one of the most basic physical processes. Rapid advances of nanofabrication techniques raise fundamental questions regarding local heating at the nanoscale [1,2]. Optical and electric heating is of particular importance in optoelectronic devices, which may lead the system out of equilibrium where the vibrational degrees of freedom as well as the electronic system cannot be described by a single temperature. In addition, the local heating and the relevant electron-phonon (e-ph) coupling are susceptible to atomic-scale defects [3–5]. Raman spectroscopy provides a unique opportunity to analyze the vibrational heating of individual modes through the ratio between the anti-Stokes and Stokes intensities. Tip-enhanced Raman spectroscopy (TERS) can achieve ultrahigh sensitivity with extremely high spatial resolution [6] and has also been applied for temperature assessment [7]. This method may allow us to visualize thermal phenomena even at the atomic scale [8,9]. However, a proper interpretation of TERS thermometry requires an in-depth understanding of microscopic heating mechanisms in a plasmonic nanojunction which are complicated by different heating channels that contribute simultaneously [10]. Here, we apply TERS thermometry to ultrathin ZnO films expitaxially grown on an Ag(111) surface [11] in order to examine the microscopic heating mechanisms and further analyze the e-ph coupling strength.

The low-temperature TERS equipment used here was reported previously [12] and detailed in Supplemental Material [13]. Figure 1(a) shows the TERS spectra obtained over a two-monolayer (ML) ZnO film on Ag(111) including both Stokes and anti-Stokes sides. The excitation wavelength (λ_{ext}) of 633 nm leads to resonance Raman scattering in which the peaks assigned to the out-of-plane and in-plane phonon modes are observed at 300–400 and 500–600 cm^{-1}, respectively [12]. The out-of-plane modes are much more intense due to the surface selection rule [27] and can be clearly observed in the anti-Stokes side, while the anti-Stokes signal of the in-plane modes is too weak for reliable analysis. Two spectra in Fig. 1(a) were recorded under the same tip conditions and at a fixed tip-surface distance (Z), but at different bias applied between the tip and the sample (V_{bias}). It is clear that the anti-Stokes intensity is significantly increased at $V_{\mathrm{bias}} = +1.75$ V. Anti-Stokes Raman scattering results from populated vibrational states, thus a larger intensity at $V_{\mathrm{bias}} = +1.75$ V indicates an elevated effective temperature given by

$$I_{\mathrm{AS}}/I_{\mathrm{S}} = A_\nu \exp(-E_\nu/k_B T_\nu), \tag{1}$$

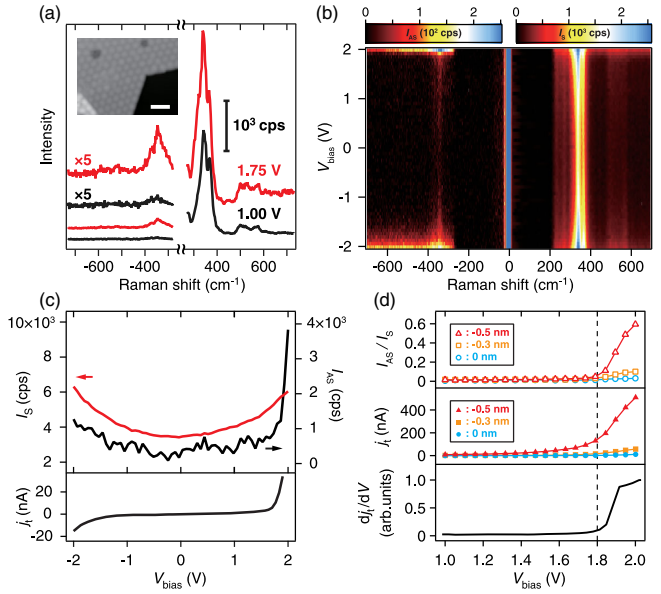

FIG. 1. (a) TERS spectra of 2-ML ZnO/Ag(111) including the Stokes (right) and anti-Stokes (left) sides ($\lambda_{ext} = 633$ nm, $F = 0.33$ mW μm^{-2}, $T_{sample} = 10$ K) at $V_{bias} = +1.00$ (black), and $+1.75$ V (red). Z is fixed at an STM set point of $V_{bias} = +1$ V, $j_t = 0.1$ nA. The inset displays an STM image of 2-ML ZnO/Ag(111) ($V_{bias} = +1$ V, $j_t = 0.1$ nA, the scale bar is 5 nm). (b) Waterfall TERS plot as a function of V_{bias} ($\lambda_{ext} = 633$ nm, $F = 0.33$ mW μm^{-2}, $T_{sample} = 10$ K). Z is fixed at an STM set point of $V_{bias} = +1$ V, $j_t = 0.1$ nA. (c) Top: TERS intensity of the out-of-plane mode as a function of V_{bias} extracted from (b), after subtraction of the continuous background. The red and black curves are I_S and I_{AS} integrated from 280 to 380 cm^{-1} and from -380 to -280 cm^{-1}, respectively. Bottom: simultaneously recorded $j_t - V_{bias}$ curve. (d) I_{AS}/I_S, j_t and dj_t/dV as a function of V_{bias} at different Z, recorded over 2-ML ZnO. The $j_t - V_{bias}$ curve is simultaneously recorded with the TERS. $Z = 0$ nm corresponds to an STM set point of $V_{bias} = +1$ V, $j_t = 0.1$ nA. The dj_t/dV spectrum measured at a set point of $V_{bias} = +1$ V, $j_t = 0.3$ nA.

where I_{AS} and I_S are the anti-Stokes and Stokes intensities, respectively, A_ν the correction factor, E_ν the vibrational energy, k_B Boltzmann constant and T_ν the effective temperature of a specific vibrational mode ν. The A_ν is unity for nonresonance Raman scattering, but it deviates when plasmonic enhancement [7] and/or electronic resonances [28] are involved. In the present case, the different plasmonic enhancement between the Stokes and anti-Stokes bands should be negligible because the Raman shift (about ± 40 meV) is much smaller compared to the spectral width of the localized surface plasmon resonance of the junction ($\sim$0.5 eV, see Fig. S1 [13]). We estimate the A_ν to be $\sim$2 by measuring the temperature dependence of the I_{AS}/I_S (Fig. S1 [13]) and obtain $T_\nu \sim 170(\pm 34)$ K and $T_\nu \sim 100(\pm 20)$ K for $V_{bias} = +1.75$ V and $+1$ V, respectively (here ν represents the out-of-plane band). Thus, the ZnO film under the tip is locally heated to a much higher T_ν than the original temperature (bulk temperature T_{sample} represents the temperature recorded at the sample stage). Note that the tip apex temperature may be much lower [13]. The T_ν is affected by the tip conditions that modify optically induced heating as discussed below. However, the general tendency of the dependence of T_ν (I_{AS}/I_S) on the measuring parameters (e.g., V_{bias} and gap distance) remains the same. Thus, the TERS thermometry here should be regarded as a measurement of local heating rather than the intrinsic temperature.

Figure 1(b) displays the V_{bias}-dependent TERS spectra recorded at a fixed Z. The top panel in Fig. 1(c) shows the I_{AS} and I_S extracted from Fig. 1(b) by integrating the peak area of the out-of-plane band. The bottom panel shows the simultaneously recorded tunneling current (j_t). The I_S exhibits a nearly quadratic dependence on the V_{bias}. Although the I_{AS} also quadratically depends on the V_{bias} below $+1.8$ V, a steep increase occurs above $+1.8$ V at which the j_t also rapidly increases due to resonant electron tunneling into the conduction band (CB) of 2-ML ZnO [11]. A continuous background in Fig. 1(b) may originate from electronic Raman scattering [29,30] or scanning tunneling luminescence [31] in the junction (Fig. S2 [13]). In Fig. 1(d), the V_{bias} dependence of I_{AS}/I_S at different Z and the simultaneously recorded j_t are plotted along with the dj_t/dV spectrum, revealing that the onset of the steep increase of the I_{AS}/I_S coincides with that in the j_t and the dj_t/dV. Although the j_t also significantly changes at $V_{bias} < -1.5$ V due to resonant tunneling to the Ag substrate states, this does not lead to a significant increase of the I_{AS}. Therefore, we conclude that the efficient heating occurs through resonant electron tunneling into the CB of 2-ML ZnO followed by subsequent e-ph coupling [32,33]. The nearly quadratic V_{bias}-dependence of both I_S and I_{AS} in Fig. 1(c) may be attributed to a change in the TERS cross section [13].

From Eq. (1) and the Planck distribution, the averaged phonon population (N_ν) can be derived from the I_{AS}/I_S by the relation of $N_\nu = 1/\{[A_\nu/(I_{AS}/I_S)] - 1\}$. As seen in Fig. 1(d) the increasing rate of the I_{AS}/I_S becomes larger at smaller Z at $V_{bias} \sim +1.8$ V. For current-induced process, the data can be fitted by $N_\nu \propto I_t^{n(V_{bias})}$, where $n(V_{bias})$ is the number of electron required to excite a specific phonon mode. The fitting result shows that $n(V_{bias})$ is changed from 0.32 to 0.92 when V_{bias} is increased from $+1.8$ to $+2$ V, respectively (Fig. S3 [13]). This sublinear $n(V_{bias})$ dependence indicates the presence of an additional optical heating channel [with $n(V_{bias}) = 0$] which competes with the tunneling current induced process [$n(V_{bias}) = 1$]. Although a sublinear $n(V_{bias})$ dependence could occur by a multiple-phonon excitation process, this is unlikely for systems adsorbed onto a metal surface due to the very short lifetime of the charged states. $n(V_{bias}) \sim 1$ at $V_{bias} = +2$ V indicates that heating is dominated by the current, where the lifetime of the phonon mode could be estimated [13].

Heating in illuminated plasmonic nanojunctions will occur either by the electric current or by optical excitation [10]. Figure 2(a) displays the waterfall plot of the TERS

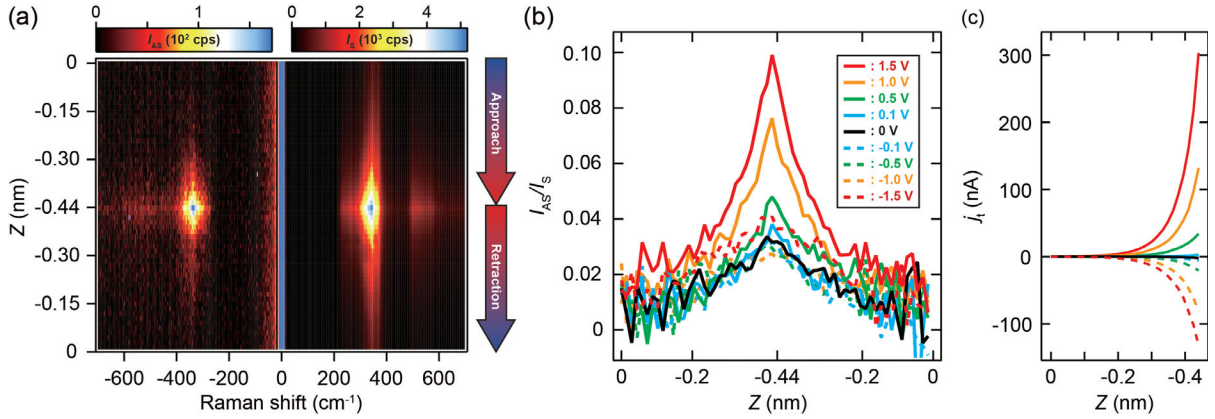

FIG. 2. (a) Waterfall TERS plot as a function of Z recorded one cycle of approach and retraction of the tip ($\lambda_{ext} = 633$ nm, $F = 0.33$ mW μm^{-2}, $T_{sample} = 10$ K). $Z = 0$ nm corresponds to an STM set point of $V_{bias} = +1$ V, $j_t = 0.1$ nA. (b) I_{AS}/I_S as a function of Z at different V_{bias}. I_S (I_{AS}) is integrated from 280 to 380 (-280 to -380) cm^{-1}. (c) Simultaneously recorded $j_t - Z$ curve.

spectra recorded for 2-ML ZnO as a function of Z, where the Ag tip approaches and retracts subsequently. Figure 2(b) shows the Z-dependent I_{AS}/I_S of the out-of-plane band measured at different V_{bias}. At all V_{bias}, the I_{AS}/I_S increases with decreasing the Z. However, the increasing rates are similar at $V_{bias} < +0.5$ V, which cannot be explained by current-induced heating because j_t is largely changed by V_{bias} [Fig. 2(c)]. Therefore, the increase in the I_{AS}/I_S at a smaller Z is associated with optically induced heating. This is further confirmed by a linear dependence of the I_{AS}/I_S on the incident laser power (Fig. S4 [13]). The increase of the I_{AS}/I_S at a small Z results from the enhancement of the plasmonic field that promotes the optically induced heating.

Figure 3 depicts possible excitation channels contributing to the heating in the Ag tip-vacuum-ZnO-Ag(111) junction under illumination. The energy level denoted as IS near the Fermi level (E_F) of Ag(111) is the interface state between 2-ML ZnO and the Ag surface, originating from the occupied Shockley state of Ag(111) [11]. The CB edge of the ZnO is positioned at 1.8 eV above E_F [11], which is pinned to E_F of Ag(111) and is not changed by V_{bias}. The heating involves four different excitation channels: in channels (1) and (2), hot electrons are first generated in the tip and the surface, respectively, through nonradiative decay of the excited localized surface plasmon and they are subsequently transferred into the CB of the ZnO from the tip or the surface. Channel (3) is direct optical excitation between the IS and the CB edge. Channel (4) is the inelastic electron tunneling (IET) process induced by V_{bias}. This channel is negligible at $V_{bias} < +1.8$ V (below the onset of CB) because off-resonant tunneling has a much smaller IET cross section. However, the increasing rate of the I_{AS}/I_S in Fig. 2(b) is larger at $V_{bias} > +1$ V (comparing to $V_{bias} < +0.5$ V) which is substantially lower than the onset bias of the CB edge. Thus, the larger increasing rate is attributed to channel (1). This is further supported by an occurrence of additional photocurrents at $V_{bias} > +1$ V (Fig. S5 [13]). However, channel (1) is inefficient at $V_{bias} < +0.5$ V as the energy difference between the CB of the ZnO and the Fermi level of the tip becomes too large [i.e., channel (1) becomes gradually operative at $V_{bias} > +0.5$ V]. Channel (2) should also be inefficient because the CB edge is located at 1.8 eV above the Fermi level, which is almost equal to the maximum energy that hot electrons can gain from the optical excitation at $\lambda_{ext} = 633$ nm and the lifetime of such high-energy hot electrons is very short (<10 fs) [34]. Therefore, the amount of electrons transferred into the CB should be very small. However, channel (3) is operative at $\lambda_{ext} = 633$ nm because the photon energy (1.9 eV) matches the electronic resonance between IS and CB [i.e., channel (3) is independent of V_{bias}]. The increase of the I_{AS}/I_S with decreasing the Z at $V_{bias} < +0.5$ V [Fig. 2(b)] is explained by the

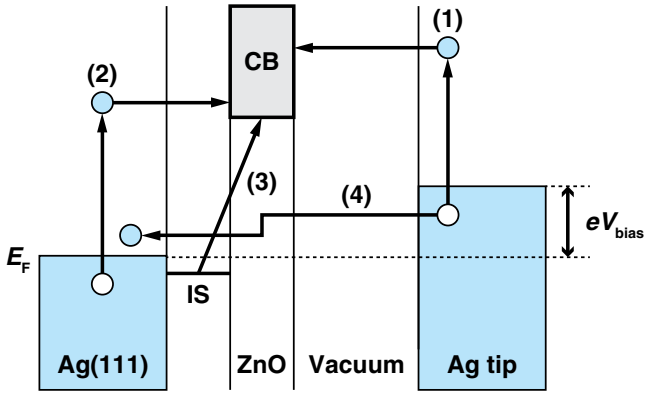

FIG. 3. Schematic of different heating channels. (1) Transfer of the photoexcited electron from the Ag tip. (2) Transfer of the photoexcited electron from the Ag(111) surface. (3) Direct optical excitation between the interface state and the conduction band. (4) Inelastic electron tunneling. E_F: Fermi level, CB: conduction band, IS: interface state.

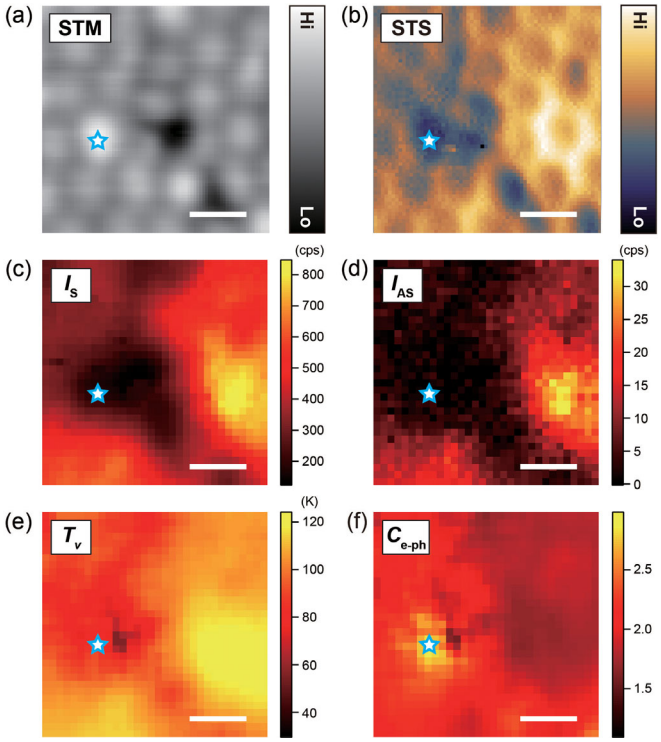

FIG. 4. (a),(b) STM ($V_{\text{bias}} = +1$ V, $j_t = 0.1$ nA) and STS of conduction band ($V_{\text{bias}} = +1.8$ V, $j_t = 1$ nA) image of 2-ML ZnO on Ag(111). The scale bar is 2 nm. (c)–(e) Mapping of I_S, I_{AS}, and T_ν of the out-of-plane phonon modes measured for the same area as (a) ($V_{\text{bias}} = +0.1$ V, $j_t = 2$ nA, $\lambda_{\text{ext}} = 633$ nm, $F = 0.34$ mW/μm^2, $t_{\text{exp}} = 3$ s, $T_{\text{sample}} = 12$ K). (f) Mapping of the relative e-ph coupling strength.

enhancement of channel (3) through the increased plasmonic field.

The high spatial resolution of TERS allows us to visualize the effect of atomic-scale inhomogeneity on the local heating. Figures 4(a) and 4(b) show the STM image of 2-ML ZnO and the scanning tunneling spectroscopy (STS) map of the CB, including atomic-scale defects that occasionally occur after voltage pulsing which may cause dropping of a tip material. We assign the bright feature marked in Fig. 4(a) to the Ag cluster. Note that the phonon frequencies and electronic structures of the 2 ML-ZnO are not significantly modified as supported by the fact that overall spectral features of TERS and STS are similar with and without the Ag cluster (see Fig. S6 [13]). The threefold symmetric protrusions in Figs. 4(a) and 4(b) represent the moiré structure resulting from the lattice mismatch between the ZnO film and the Ag(111) surface [35]. The STS map [Fig. 4(b)] shows that the local density of states (LDOS) of the CB is modulated by the Ag cluster. As mentioned above, because $\lambda_{\text{ext}} = 633$ nm leads to resonant Raman scattering for 2-ML ZnO, the TERS intensity is strongly correlated with the LDOS [12]. Figures 4(c) and 4(d) display the map of I_S and I_{AS}, respectively, recorded in the constant-current STM mode. The Ag cluster should be located on the ZnO surface. This will modulate the CB of the ZnO layer but the IS will remain intact. Thus, the transition matrix element between the IS and the CB is affected exclusively by the modification of the CB. This is also implicated by a larger (smaller) TERS intensity at the positions exhibiting higher (lower) LDOS of the CB in the STS map. However, the TERS intensities are not correlated with the simultaneously recorded STM topography (Fig. S6). This excludes the possibility that the TERS contrast is caused by a change in the tip height. Figure 4(b) reveals that the LDOS variation of the CB at the <1 nm scale is comparable or smaller than the size of the plasmonic field in the STM junction which determines the spatial resolution of TERS [12]. Figure S7 [13] shows the spatially averaged STS map of Fig. 4(b) with a mean filter of a 2-nm diameter, revealing a similar appearance as the TERS map in Figs. 4(c) and 4(d), corroborating that the field confinement is ~2 nm. Figure 4(e) shows the T_ν map for 2-ML ZnO obtained from Figs. 4(c) and 4(d), which also exhibit a similar appearance as the averaged STS map. According to the heating mechanism discussed above, when the TERS mapping is recorded at $V_{\text{bias}} = +0.1$ V, the ZnO film is heated mainly through direct optical absorption of the confined field, i.e., via channel (3) in Fig. 3. In this case, a higher T_ν is expected for the positions with larger LDOS because more efficient local optical absorption between the IS and the CB is expected. Note that the optical heating as well as the TERS intensity is susceptible to a change in the field enhancement in the junction. However, this contribution is expected to be small because the separation distance between the tip apex and the Ag surface remains almost constant during the measurement (Fig. S6 [13]) and we ignore it in the discussion below. The spatial resolution of the T_ν map (~2 nm) is determined by the size of the confined field, but the actual heated area will be larger than the size of the field because of lateral heat transfer. Additional data for a domain boundary and a line defect are shown in Fig. S8 [13], which further confirms the correlation between the T_ν and the LDOS of the CB. We also examined local heating over 3-ML ZnO films having a resonant excitation wavelength of $\lambda_{\text{ext}} = 780$ nm [11], but the TERS intensity is much weaker than that for 2-ML ZnO, hampering the TERS thermometry.

TERS thermometry also provides a unique possibility to assess a local e-ph coupling strength. When the ZnO film under the tip is locally heated, the generated heat will be transferred to the surrounding. The heat transfer satisfies the relationship $J \sim K[T_\nu(r) - T_0] \sim \mathrm{A}(r)C_{e\text{-ph},\nu}(r)$, where J is the heat flow, K the heat transfer coefficient, r the tip position, $T_\nu(r)$ the temperature of the ZnO film under the tip, T_0 the environment temperature, $A(r)$ the absorption coefficient, $C_{e\text{-ph},\nu}(r)$ the e-ph coupling strength of vibrational mode v. The $A(r)$ is proportional to the LDOS of the CB, $\rho(r)$ because the LDOS of the IS is expected to be spatially homogeneous. The vertical heat transfer (to the

substrate) is not affected as long as the interface remains intact and the phonon frequencies of 2-ML ZnO in TERS are not significantly influenced by the inhomogeneity (Fig. S6 [13]). The latter suggests that the lattice properties are unchanged and the lateral heat transfer within the ZnO film will be weakly dependent on the position. Therefore, we assume that K is spatially homogeneous (treated as a constant). Then the e-ph coupling strength at a specific position can be estimated from the T_ν and the LDOS of the CB (STS map) using the relationship of $C_{e\text{-ph},\nu}(r) \propto [T_\nu(r) - T_0]/\rho(r)$. Figure 4(f) shows the map of the relative e-ph coupling strength for the out-of-plane modes obtained by dividing T_ν [Fig. 4(e)] with the filtered STS map in Fig. S7 [13]. The $C_{e\text{-ph},\nu}(r)$ is higher at the Ag cluster position, while it exhibits a much smaller variation over the intact ZnO film. Under illumination, transient charging of the Ag cluster may occur due to the increase of the LDOS below the CB of the ZnO (acting as a dopant level, see Fig. S6a [13]), promoting e-ph coupling as observed in a localized donor in a bulk ZnO [36]. The simple model we employed here is valid only for a qualitative evaluation of a relative e-ph coupling strength. Our approach will pave the way for tracing local electron-phonon coupling dynamics in real space and real time at the atomic-scale resolution by combining it with time-resolved Raman spectroscopy [37].

The authors thank Adnan Hammud for providing the Ag tips fabricated by using focused ion beam. This work was supported by JSPS KAKENHI Grant No. 19K24684.

*Corresponding author.
kuma@ims.ac.jp

[1] D. G. Cahill, W. K. Ford, K. E. Goodson, G. D. Mahan, A. Majumdar, H. J. Maris, R. Merlin, and S. R. Phillpot, Nanoscale thermal transport, J. Appl. Phys. **93**, 793 (2003).
[2] E. Pop, Energy dissipation and transport in nanoscale devices, Nano Res. **3**, 147 (2010).
[3] M. Hase and M. Kitajima, Interaction of coherent phonons with defects and elementary excitations, J. Phys. Condens. Matter **22**, 073201 (2010).
[4] N. Yazdani, S. Volk, O. Yarema, M. Yarema, and V. Wood, Size, ligand, and defect-dependent electron-phonon coupling in chalcogenide and perovskite nanocrystals and its impact on luminescence line widths, ACS Photonics **7**, 1088 (2020).
[5] S. Smairat and J. Grahama, Vacancy-induced enhancement of electron-phonon coupling in cubic silicon carbide and its relationship to the two-temperature model, J. Appl. Phys. **130**, 125902 (2021).
[6] R. Zhang *et al.*, Chemical mapping of a single molecule by plasmon-enhanced Raman scattering, Nature (London) **498**, 82 (2013).
[7] M. Richard-Lacroix and V. Deckert, Direct molecular-level near-field plasmon and temperature assessment in a single plasmonic hotspot, Light Sci. Appl. **9**, 35 (2020).
[8] J. Lee, K. T. Crampton, N. Tallarida, and V. A. Apkarian, Visualizing vibrational normal modes of a single molecule with atomically confined light, Nature (London) **568**, 78 (2019).
[9] Y. Zhang *et al.*, Visually constructing the chemical structure of a single molecule by scanning Raman picoscopy, Natl. Sci. Rev. **6**, 1169 (2019).
[10] D. R. Ward, D. A. Corley, J. M. Tour, and D. Natelson, Vibrational and electronic heating in nanoscale junctions, Nat. Nanotechnol. **6**, 33 (2011).
[11] T. Kumagai, S. Liu, A. Shiotari, D. Baugh, S. Shaikhutdinov, and M. Wolf, Local electronic structure, work function, and line defect dynamics of ultrathin epitaxial ZnO layers on a Ag(111) surface, J. Phys. Condens. Matter **28**, 494003 (2016).
[12] S. Liu, M. Müller, Y. Sun, I. Hamada, A. Hammud, M. Wolf, and T. Kumagai, Resolving the correlation between tip-enhanced resonance Raman scattering and local electronic states with 1 nm resolution, Nano Lett. **19**, 5725 (2019).
[13] See Supplemental Material at http://link.aps.org/supplemental/10.1103/PhysRevLett.128.206803 for experimental details, estimation of the correction factor, tip apex temperature under illumination, V_{bias} dependence of the continuous background in the TERS spectra, V_{bias} dependence of the I_S and I_{AS}, dependence of the vibrational population on the tunneling current, dependence of I_{AS}/I_S on the incident laser power, $j_t - V_{\text{bias}}$ curve with and without illumination, STS and TERS spectra over the Ag cluster, filtered STS mapping, TERS mapping including edges and a line defect in 2-ML ZnO, local heating for 3-ML ZnO films, which includes Refs. [14–26].
[14] Q. Pan, B. H. Liu, M. E. McBriarty, Y. Martynova, I. M. N. Groot, S. Wang, M. J. Bedzyk, S. Shaikhutdinov, and H.-J. Freund, Reactivity of ultra-thin ZnO films supported by Ag(111) and Cu(111): A comparison to ZnO/Pt(111), Catal. Lett. **144**, 648 (2014).
[15] H. Böckmann, S. Liu, M. Müller, A. Hammud, M. Wolf, and T. Kumagai, Near-field manipulation in a scanning tunneling microscope junction with plasmonic Fabry-Pérot tips, Nano Lett. **19**, 3597 (2019).
[16] Z. Ioffe, T. Shamai, A. Ophir, G. Noy, I. Yutsis, K. Kfir, O. Cheshnovsky, and Y. Selzer, Detection of heating in current-carrying molecular junctions by Raman scattering, Nat. Nanotechnol. **3**, 727 (2008).
[17] R. L. M. Gieseking, J. Lee, N. Tallarida, V. A. Apkarian, and G. C. Schatz, Bias-dependent chemical enhancement and nonclassical stark effect in tip-enhanced Raman spectromicroscopy of CO-terminated Ag tips, J. Phys. Chem. Lett. **9**, 3074 (2018).
[18] S. Kaneko, K. Yasuraoka, and M. Kiguchi, Bias voltage induced surface-enhanced Raman scattering enhancement on the single-molecule junction, J. Phys. Chem. C **123**, 6502 (2019).
[19] K. Ikeda, S. Suzuki, and K. Uosaki, Enhancement of SERS background through charge transfer resonances on single crystal gold surfaces of various orientations, J. Am. Chem. Soc. **135**, 17387 (2013).
[20] S. Liu, A. Hammud, M. Wolf, and T. Kumagai, Anti-stokes light scattering mediated by electron transfer across a biased plasmonic nanojunction, ACS Photonics **8**, 2610 (2021).

[21] D. C. Marinica, M. Zapata, P. Nordlander, A. K. Kazansky, P. M. Echenique, J. Aizpurua, and A. G. Borisov, Active quantum plasmonics, Sci. Adv. **1**, e1501095 (2015).
[22] D. Feng, Y. Feng, S. Yuan, X. Zhang, and G. Wang, Melting behavior of Ag nanoparticles and their clusters, Appl. Therm. Eng. **111**, 1457 (2017).
[23] W. Ho, Single-molecule chemistry, J. Chem. Phys. **117**, 11033 (2002).
[24] R. Cuscó, Esther Alarcón-Lladó, Jordi Ibáñez, Luis Artús, Juan Jiménez, Buguo Wang, and Michael J. Callahan, Temperature dependence of Raman scattering in ZnO, Phys. Rev. B **75**, 165202 (2007).
[25] S. Liu, M. Wolf, and T. Kumagai, Plasmon-Assisted Resonant Electron Tunneling in a Scanning Tunneling Microscope Junction, Phys. Rev. Lett. **121**, 226802 (2018).
[26] S. Liu, B. Cirera, Y. Sun, I. Hamada, M. Müller, A. Hammud, M. Wolf, and T. Kumagai, Dramatic enhancement of tip-enhanced Raman scattering mediated by atomic point contact formation, Nano Lett. **20**, 5879 (2020).
[27] M. Moskovits and J. S. Suh, Surface selection rules for surface-enhanced Raman spectroscopy: Calculations and application to the surface-enhanced Raman spectrum of phthalazine on silver, J. Phys. Chem. **88**, 5526 (1984).
[28] M. Oron-Carl and R. Krupke, Raman Spectroscopic Evidence for Hot-Phonon Generation in Electrically Biased Carbon Nanotubes, Phys. Rev. Lett. **100**, 127401 (2008).
[29] S. Mahajan, R. M. Cole, J. D. Speed, S. H. Pelfrey, A. E. Russell, P. N. Bartlett, S. M. Barnett, and J. J. Baumberg, Understanding the surface-enhanced Raman spectroscopy "background," J. Phys. Chem. C **114**, 7242 (2010).
[30] J. T. Hugall and J. J. Baumberg, Demonstrating photoluminescence from Au is electronic inelastic light scattering of a plasmonic metal: The origin of SERS backgrounds, Nano Lett. **15**, 2600 (2015).
[31] F. Rossel, M. Pivetta, and W.-D. Schneider, Luminescence experiments on supported molecules with the scanning tunneling microscope, Surf. Sci. Rep. **65**, 129 (2010).
[32] B. N. J. Persson and A. Baratoff, Inelastic Electron Tunneling from a Metal Tip: The Contribution from Resonant Processes, Phys. Rev. Lett. **59**, 339 (1987).
[33] M. Galperin, M. A. Ratner, and A. Nitzan, Raman scattering in current-carrying molecular junctions, J. Chem. Phys. **130**, 144109 (2009).
[34] M. Bauer, A. Marienfeld, and M. Aeschlimann, Hot electron lifetimes in metals probed by time-resolved two-photon photoemission, Prog. Surf. Sci. **90**, 319 (2015).
[35] A. Shiotari, B. H. Liu, S. Jaekel, L. Grill, S. Shaikhutdinov, H.-J. Freund, M. Wolf, and T. Kumagai, Local characterization of ultrathin ZnO layers on Ag(111) by scanning tunneling microscopy and atomic force microscopy, J. Phys. Chem. C **118**, 27428 (2014).
[36] H. Zheng, J. Kröger, and R. Berndt, Spectroscopy of Single Donors at ZnO(0001) Surfaces, Phys. Rev. Lett. **108**, 076801 (2012).
[37] V. Kozich and W. Werncke, The vibrational pumping mechanism in surface-enhanced Raman scattering: A subpicosecond time-resolved study, J. Phys. Chem. C **114**, 10484 (2010).